The Astrophysical Journal Supplement Series, 283:12 (15pp), 2026 March https://doi.org/10.3847/1538-4365/ae3bc9

Searching for Solar-like Oscillations Using TESS 2 minute Cadence in the Southern Ecliptic Hemisphere

Yezheng Feng[1,2], Tao Wu[1,2,3,4,5,6], Hui-Fang Xue[7,8,9], Feiyang Li[2,5], and Jia-Shu Niu[1,10,11]
[1] Institute of Theoretical Physics, Shanxi University, Taiyuan 030006, People's Republic of China; wutao@ynao.ac.cn, jsniu@sxu.edu.cn
[2] Yunnan Observatories, Chinese Academy of Sciences, 396 Yangfangwang, Guandu District, Kunming 650216, People's Republic of China
[3] Center for Astronomical Mega-Science, Chinese Academy of Sciences, 20A Datun Road, Chaoyang District, Beijing 100012, People's Republic of China
[4] Key Laboratory for the Structure and Evolution of Celestial Objects, Chinese Academy of Sciences, 396 Yangfangwang, Guandu District, Kunming 650216, People's Republic of China
[5] University of Chinese Academy of Sciences, Beijing 100049, People's Republic of China
[6] International Centre of Supernovae (ICESUN), Yunnan Key Laboratory of Supernova Research, Kunming 650216, People's Republic of China
[7] Department of Physics, Taiyuan Normal University, Jinzhong 030619, People's Republic of China
[8] Institute of Computational and Applied Physics, Taiyuan Normal University, Jinzhong 030619, People's Republic of China
[9] Shanxi Key Laboratory for Intelligent Optimization Computing and Blockchain Technology, Jinzhong 030619, People's Republic of China
[10] State Key Laboratory of Quantum Optics Technologies and Devices, Shanxi University, Taiyuan 030006, People's Republic of China
[11] Collaborative Innovation Center of Extreme Optics, Shanxi University, Taiyuan 030006, People's Republic of China

Received 2024 November 15; revised 2026 January 16; accepted 2026 January 19; published 2026 February 25

Abstract

The TESS space mission has generated an extensive collection of light curves, providing a valuable opportunity to search for solar-like oscillations. Numerous studies have utilized TESS observations to search for solar-like oscillations and achieved excellent results. However, the number of oscillators found by the previous works may be incomplete and significantly below the predicted count. Therefore, we employed a novel method to search for solar-like oscillations. In this work, we utilized TESS 2 minute cadence data to identify solar-like oscillators in the southern ecliptic hemisphere, detecting the presence of oscillations by identifying an excess power hump in the spectrum and combining visual inspection. As a result, we identified 10,548 stars exhibiting solar-like oscillations including 2972 that had not been reported in previous studies. The $\nu_{\max}$ and $\Delta\nu$ of oscillators were determined using the fitting and autocorrelation, and the reliability of the $\Delta\nu$ measurements was further evaluated using the Fourier spectrum of the autocorrelation function. Based on this assessment, 4775 oscillators were classified as having reliable $\Delta\nu$, including 1920 that have $\Delta\nu$ measured for the first time.

Unified Astronomy Thesaurus concepts: Asteroseismology (73); Red giant stars (1372); Light curves (918)

1. Introduction

Asteroseismology is a powerful tool for probing stellar internal structures and evolutionary stages, enabling the precise determination of fundamental stellar parameters such as mass, radius, surface gravity, and age through the oscillation waves that penetrate stellar interiors. Solar-like oscillations are pressure-mode oscillations excited by stochastic convection in the outer layers of the stellar surface, the same as the excitation mechanism of the solar 5 minute oscillations. Solar-like oscillations are hosted by stars with outer convection zones and are therefore prevalent in lower main sequence (MS) stars, subgiants (SG), and stars on the red giant branch (RGB), horizontal branch, and asymptotic giant branch (refer to S. Joshi & Y. C. Joshi 2015).

Solar-like oscillators are most commonly studied in the frequency domain, via the observed power spectral density (PSD). The signature of solar-like oscillations in PSD consists of several sharp peaks, often described using Lorentzian functions, at individual mode frequencies. The amplitudes of these peaks are modulated by a roughly Gaussian distribution, the mean of which is $\nu_{\max}$. Each peak corresponds to an individual oscillation mode. The radial dependence of a mode of oscillation is identified with its radial order, n. The horizontal dependence of the oscillation modes is approximated by spherical harmonic functions, and so each overtone is also identified by its angular degree, l. The separation in frequency between modes with the same angular degrees l and consecutive radial order n for pressure modes is approximately constant, known as the large frequency spacing $\Delta\nu$. It is worth noting that a complete identification of a mode requires a third quantum number—the azimuthal order m. However, when the frequency resolution is insufficient and the stellar rotation is slow, the m components generally remain degenerate and cannot be individually resolved. Combined with the effective temperature, stars exhibiting solar-like oscillations can have their parameters such as mass, radius, luminosity, and surface gravity calculated through scaling relations derived from their oscillation characteristics (H. Kjeldsen & T. R. Bedding 1995; D. Stello et al. 2009; T. Kallinger et al. 2010b; T. R. White et al. 2011; E. P. Bellinger 2019; E. P. Bellinger et al. 2019).

In the past two decades, thanks to high-precision space telescopes such as CoRoT (A. Baglin et al. 2006), Kepler (W. J. Borucki et al. 2010), and K2 (S. B. Howell et al. 2014), over 100,000 solar-like oscillators have been discovered (S. Hekker et al. 2009, 2011; B. Mosser et al. 2010; D. Huber et al. 2011, 2014; D. Stello et al. 2013, 2017; S. Mathur et al. 2016; J. Yu et al. 2016). The TESS mission (G. R. Ricker et al. 2015) launched by NASA in 2018 has provided a wealth of light curves, giving us the opportunity to search for solar-like oscillations across the entire sky. Recently, numerous studies have attempted to search for solar-like oscillators using

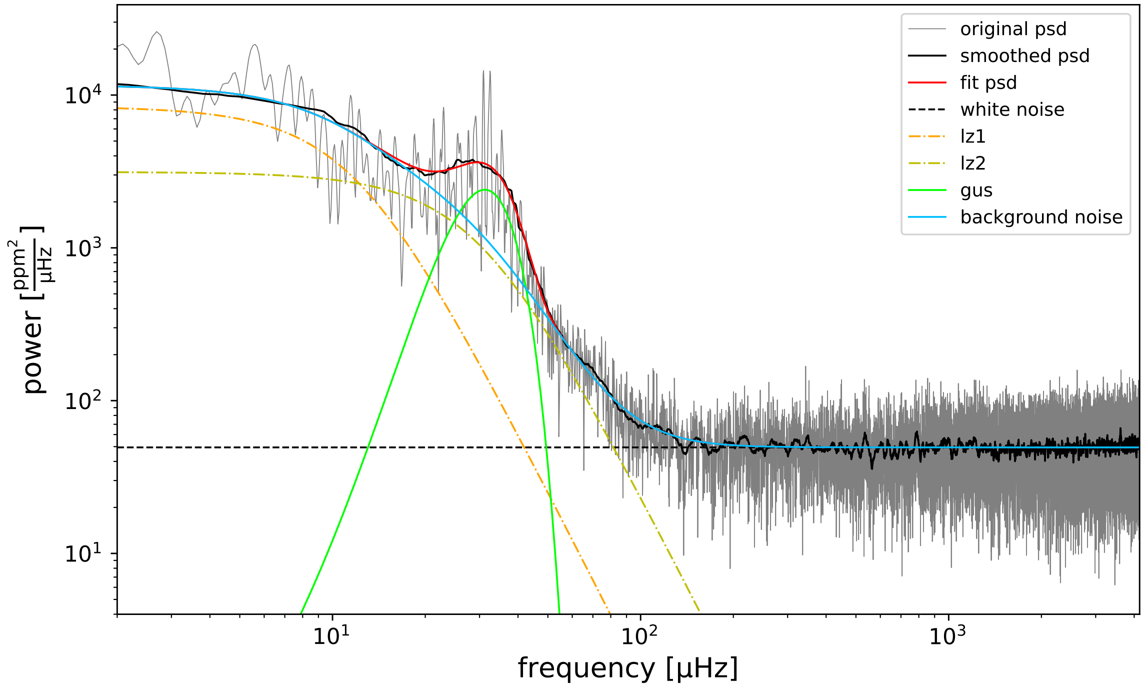

Figure 1. PSD of TIC 469248308. The gray shading represents the original PSD, while the black solid line depicts the median-smoothed PSD with a window width of $4\Delta\nu_{\mathrm{expect}}$. The red solid line illustrates the fit of the smoothed PSD using Equation (7), and the green solid line corresponds to the Gaussian function fitted to the excess power hump. The dashed lines in three distinct colors represent the three background noise components, with the blue solid line indicating the total background component.

TESS observations. For instance, D. Stello et al. (2022) identified approximately 4500 oscillating red giants within the Kepler field. M. Hon et al. (2021) employed machine learning techniques to discover 158,000 solar-like oscillators using 30 minute cadence data across the entire TESS field. E. Hatt et al. (2023) employed a probabilistic approach (see M. B. Nielsen et al. 2022) that focuses on SG and MS stars for the detection of solar-like oscillations, identifying 4177 oscillators in the TESS 2 minute cadence data from observation of Sectors 1 to 46. J. Zhou et al. (2024) identified 8651 oscillators by utilizing the autocorrelation function (ACF) to detect regularly spaced overtone in the spectrum, using 2 minute cadence light curves from Sectors 1 to 60.

Based on a preliminary simulation of the full TESS sky (TESS General Investigator Proposal No. G011188), TESS is expected to detect oscillators in 500,000 red giants (V. Silva Aguirre et al. 2020), which is a far larger count than in the aforementioned catalogs. Although the previous research has yielded significant results, the number of solar-like oscillators identified using TESS data is far below both the projections. D. Stello et al. (2022) visually inspected spectra from TESS full-frame images for more than 8000 Kepler oscillating red giants and identified oscillations in about 3000 stars, with $\Delta\nu$ measurable in only ~20% (570 oscillators) of them. This suggests that methods relying on the regular repeating patterns, such as those used in E. Hatt et al. (2023) and J. Zhou et al. (2024), may lead to many oscillators being missed. Therefore, we aimed to identify a larger number of solar-like oscillators using methods that do not rely on the detection of the large frequency spacing. In this work, we identified the presence of an excess power hump in the spectrum to search for solar-like oscillations, combining visual inspection.

2. Previous Experience

For solar-like oscillations, $\nu_{\max}$ and $\Delta\nu$ are related to stellar mass M, radius R, and effective temperature T_{eff}, and expressed as follows (H. Kjeldsen & T. R. Bedding 1995):

$$\Delta\nu \approx \sqrt{\frac{M/M_\odot}{(R/R_\odot)^3}}\,\Delta\nu_\odot, \tag{1}$$

$$\nu_{\max} \approx \frac{M/M_\odot}{(R/R_\odot)^2\sqrt{T_{\mathrm{eff}}/T_{\mathrm{eff},\odot}}}\,\nu_{\max,\odot}, \tag{2}$$

where $T_{\mathrm{eff},\odot} = 5777$ K, $\nu_{\max,\odot} = 3120\,\mu$Hz, and $\Delta\nu_\odot = 134.88\,\mu$Hz (T. Kallinger et al. 2010a; S. Hekker 2020). Combining with T_{eff}, the stellar mass, radius, and surface gravity can be calculated as follows:

$$\frac{M}{M_\odot} \approx \left(\frac{\Delta\nu}{f_{\Delta\nu}\,\Delta\nu_\odot}\right)^{-4}\left(\frac{\nu_{\max}}{f_{\nu_{\max}}\,\nu_{\max,\odot}}\right)^{3}\left(\frac{T_{\mathrm{eff}}}{T_{\mathrm{eff},\odot}}\right)^{3/2}, \tag{3}$$

$$\frac{R}{R_\odot} \approx \left(\frac{\Delta\nu}{f_{\Delta\nu}\,\Delta\nu_\odot}\right)^{-2}\left(\frac{\nu_{\max}}{f_{\nu_{\max}}\,\nu_{\max,\odot}}\right)\left(\frac{T_{\mathrm{eff}}}{T_{\mathrm{eff},\odot}}\right)^{1/2}, \tag{4}$$

$$\frac{g}{g_\odot} \approx \left(\frac{\nu_{\max}}{f_{\nu_{\max}}\,\nu_{\max,\odot}}\right)\left(\frac{T_{\mathrm{eff}}}{T_{\mathrm{eff},\odot}}\right)^{1/2}, \tag{5}$$

where $f_{\Delta\nu}$ and $f_{\nu_{\max}}$ are correction factors. Different studies have proposed various correction models (S. Sharma et al. 2016; L. S. Viani et al. 2017; S. Hekker 2020; T. Li et al. 2022). According to the prescription of S. Sharma et al. (2016), the correction factors depend on stellar properties such as effective temperature, mass, metallicity, and evolutionary stage.

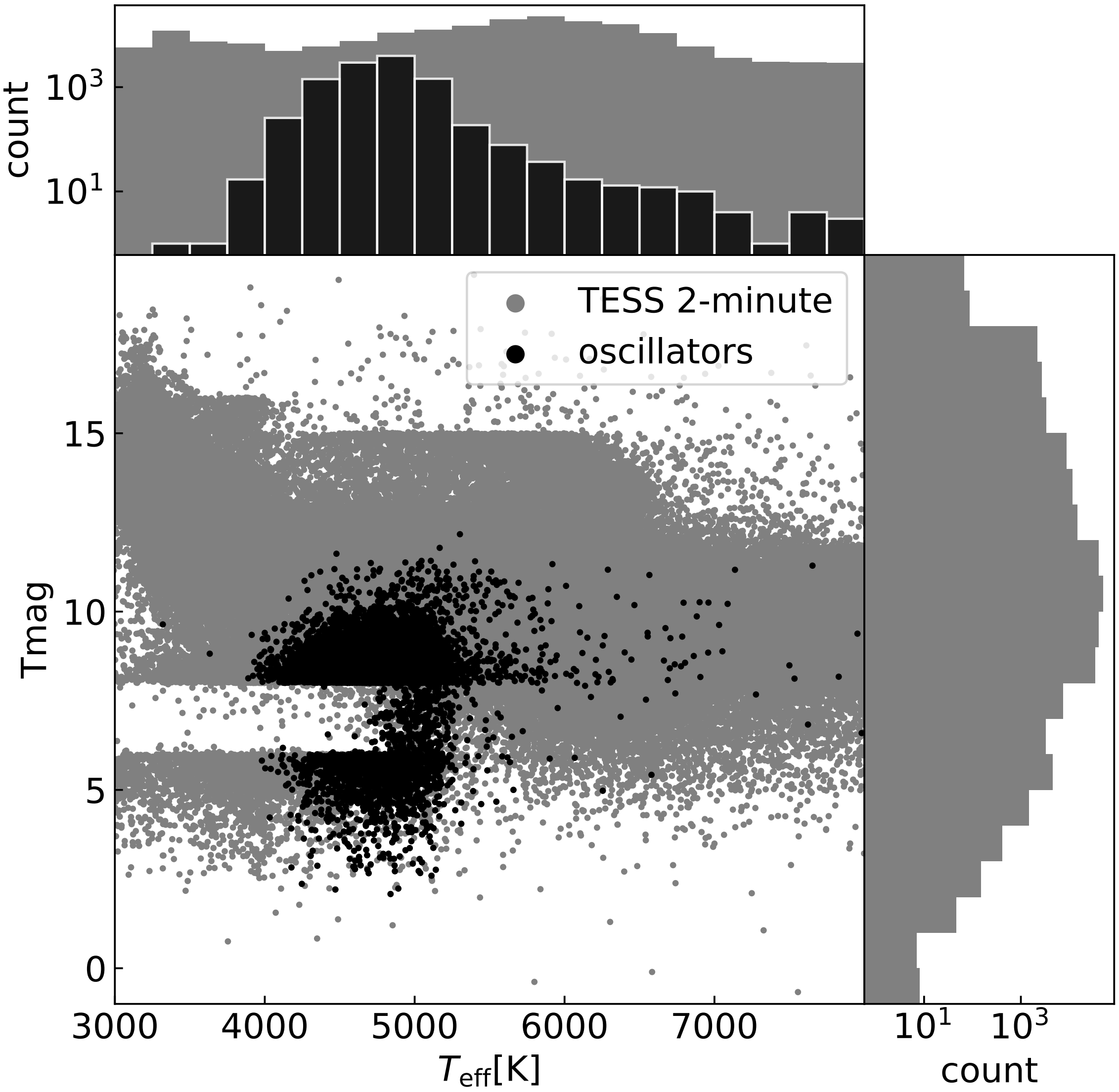

Figure 2. The central panel displays the distribution of sample stars in terms of effective temperature and TESS magnitude. Gray dots represent all target stars, while black dots indicate solar-like oscillators were found in this work. The top panel shows the distribution of stars by $T_{\rm eff}$, and right panel illustrates the distribution of stars by $T_{\rm mag}$.

S. Hekker et al. (2009) fitted the relationship between $\nu_{\rm max}$ and $\Delta\nu$ based on a sample of red giants and obtained the following results:

$$\Delta\nu = \Delta\nu_{\odot} \cdot (\nu_{\rm max}/\nu_{{\rm max},\odot})^{0.784\pm0.003}. \tag{6}$$

As shown in Figure 1, the PSD of solar-like oscillators can be modeled as the sum of a constant term representing white noise, multiple Lorentzian-like components describing backgrounds varying with frequency (caused by stellar activity, granulation, etc.), and a Gaussian function that captures the excess power hump (J. Harvey 1985; C. Jiang et al. 2011; T. Wu et al. 2014). The formula is as follows

$$P(\nu) = P_n + \sum_{i=1}^{2} \frac{4\sigma_i^2 \tau_i}{1 + (2\pi\nu\tau_i)^2 + (2\pi\nu\tau_i)^4} + D\exp\left(\frac{-(\nu_{\rm max} - \nu)^2}{2\sigma_g^2}\right), \tag{7}$$

where σ_i is the rms intensity, τ_i is the characteristic timescale, D represents the height at the central frequency of the Gaussian function, and σ_g is the standard deviation of the Gaussian function.

3. Target Selection

We selected approximately 220,000 stars observed by TESS with 2 minute cadence in the southern ecliptic hemisphere during its first and third years (covering Sectors 1 to 13 and 27 to 39[12]) as our sample. No additional constraints were imposed on the stellar parameters.

The distribution of these stars in terms of effective temperature $T_{\rm eff}$ and TESS magnitude $T_{\rm mag}$ is illustrated in Figure 2. As shown in the central panel of Figure 2, there is a marked decline in the number of stars with $T_{\rm mag}$ between 6 and 8 at temperatures below 5000 K. This may be due to the target selection criteria of the TESS mission (K. G. Stassun et al. 2018, 2019). The position of the sample on the Hertzsprung–Russell (H-R) diagram is depicted in Figure 3.

---

[12] https://tess.mit.edu/public/target_lists/target_lists.html

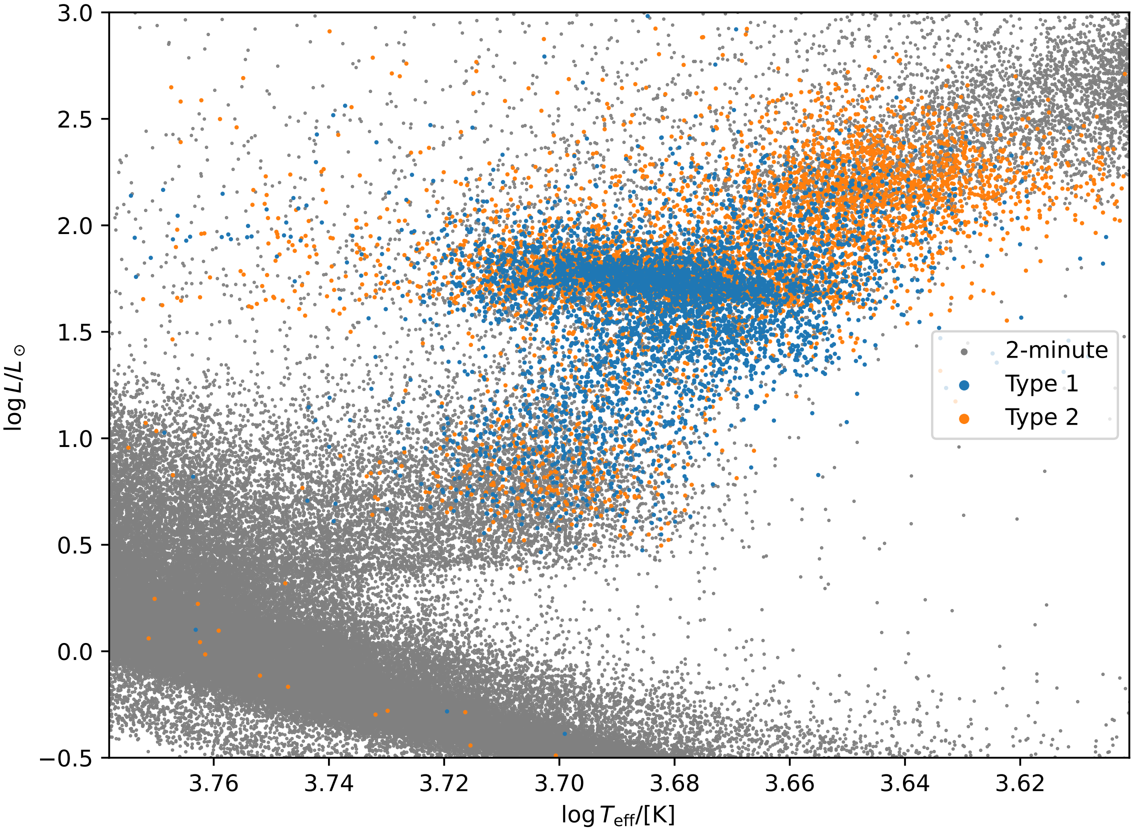

Figure 3. Positions of solar-like oscillators identified in this work on the Hertzsprung–Russell diagram. Gray points represent all sample stars. The blue and orange dots indicate oscillators classified as "type 1" and "type 2," respectively. The luminosity is estimated using the radius and effective temperature provided in the TESS Input Catalog, based on the Stefan–Boltzmann relation.

4. The Search Process and Methods

4.1. Obtaining Power Spectral Density

We utilized the Lightkurve[13] Python package (Lightkurve Collaboration et al. 2018; A. Ginsburg et al. 2019; Astropy Collaboration et al. 2022) to download the PDC-SAP light curves, which were processed by the TESS Science Processing Operations Center pipeline. For each sector, the light curve was normalized by its median value. The Lomb–Scargle algorithm, which is designed for Fourier transformation in the context of unevenly sampled data (N. R. Lomb 1976; J. D. Scargle 1982; J. T. VanderPlas 2018), was applied to obtain the PSD.

Unlike Kepler, which provided nearly continuous coverage, TESS observes each sector for only 27 days. Owing to the TESS observing strategy, a given target may be covered in multiple sectors, resulting in long gaps in its light curve, which introduce complex side lobes and affect power value in the PSD. To mitigate these effects, we computed the PSD using the method described by T. R. Bedding & H. Kjeldsen (2022). The PSD was computed by first defining a frequency axis from 2 to 4166 μHz with a step of $0.429/5$ μHz. Then, PSDs were calculated for each sector of the same target and then averaged to obtain the final PSD. Here, 4166 μHz represents the Nyquist frequency of the 2 minute cadence, 0.429 μHz corresponds to the frequency resolution for a 27 day observation, and an oversampling factor of 5 was applied.

4.2. Excess Power-hump Fitting

To identify solar-like oscillations through the detection of the excess power hump, it is necessary to characterize the properties of this feature. According to Equation (7), the excess power hump can be modeled by a Gaussian function, whose shape is determined by $\nu_{\rm max}$, D, and σ_g. Therefore, we fitted Equation (7) to the PSDs of 2749 oscillators detected by E. Hatt et al. (2023) in the southern ecliptic hemisphere, allowing us to derive the empirical dependence of D and σ_g on $\nu_{\rm max}$.

The fitting was carried out as follows. The PSD was first smoothed with a moving-average filter using a window of $4\Delta\nu_\odot \cdot (\nu_{\rm max}/\nu_{{\rm max},\odot})^{0.784}$ (S. Hekker et al. 2009). Then, we performed a least-squares fit after taking the logarithm of both Equation (7) and the smoothed PSD. Furthermore, the fit was restricted to frequencies below $2\nu_{\rm max} + 300$ μHz, which reduces the computational cost without sacrificing the oscillation features for the fitting. Finally, we visually inspected the fitting results and excluded a small number of stars for which the Gaussian envelope was either not visible in the spectrum or the Gaussian component deviated significantly from the envelope due to the fitting parameters becoming trapped in a local minimum. The distributions of D and σ_g as a function of $\nu_{\rm max}$ for the remaining 2688 stars are shown in Figures 4(a) and (b). As shown in the figure, $\log D$ exhibits an approximately linear relation with $\log \nu_{\rm max}$. However, a slight change in the intercept is observed around $\log \nu_{\rm max} \approx 2.1$. To account for the fact that the $\nu_{\rm max}$–D relation differs for stars in different evolutionary stages, we employed a piecewise linear function with a break point at $\log \nu_{\rm max} = 2.1$ to fit the relation

---

[13] https://lightkurve.github.io/lightkurve/

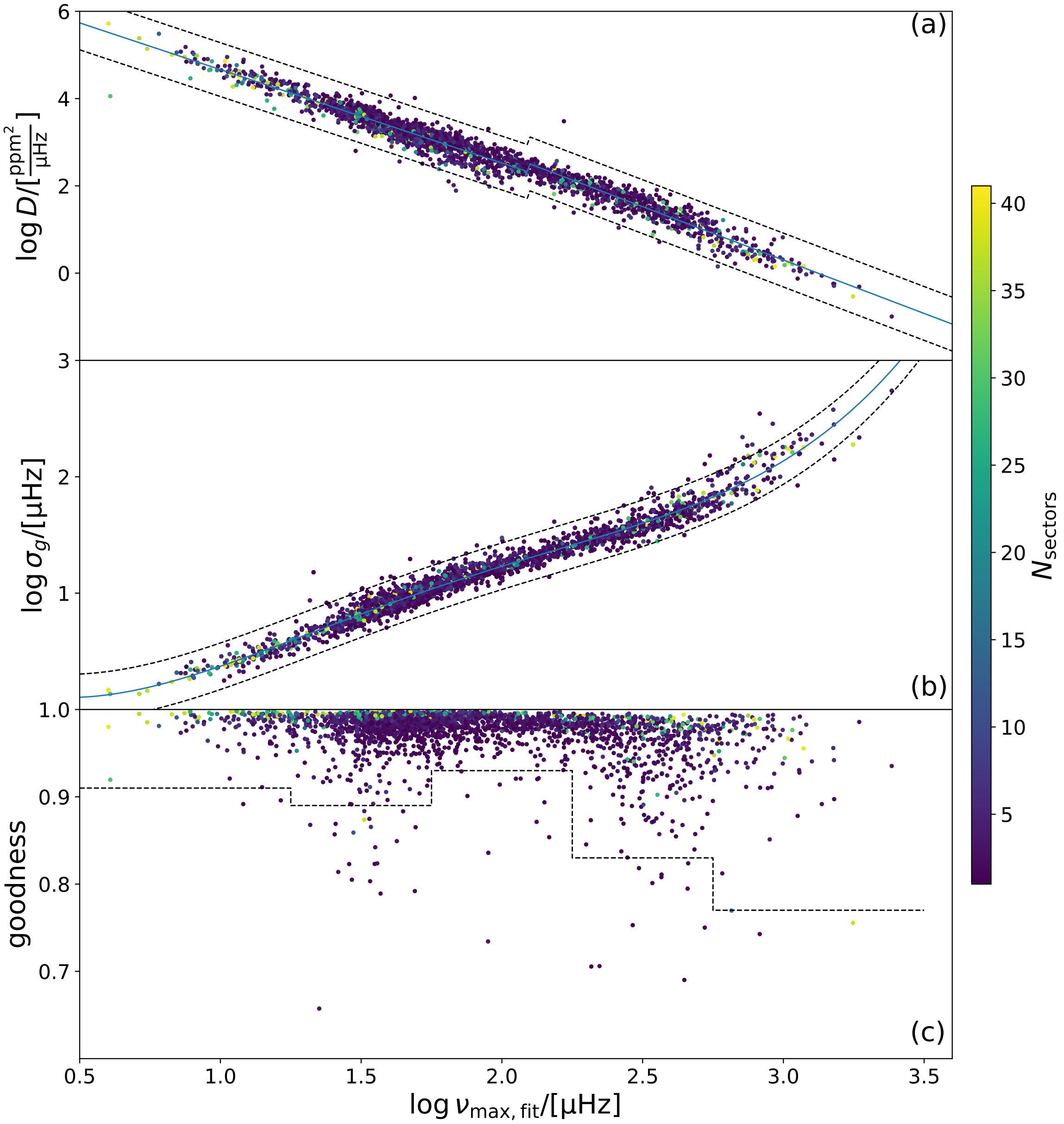

Figure 4. Distributions of $\log D$ (a), $\log \sigma_g$ (b), and the goodness of fit (c) as functions of $\nu_{\max}$. The blue solid lines denote the fitted relations. Dashed lines in panels (a) and (b) indicate the fitted function offset by $\pm 3\sigma$ of the residuals. The dashed line in panel (c) indicates the 2nd percentile of the goodness-of-fit values within each $\log \nu_{\max}$ interval (98% lie above). The bin boundaries are 0.5, 1.25, 1.75, 2.25, 2.75, and 3.5.

between $\log D$ and $\log \nu_{\max}$. The resulting fit is indicated by the blue solid line in Figure 4(a):

$$\log D = \begin{cases} (6.81 \pm 0.03) - (2.14 \pm 0.02) \log \nu_{\max}, & \log \nu_{\max} \leqslant 2.1 \\ (7.64 \pm 0.08) - (2.45 \pm 0.03) \log \nu_{\max}, & \log \nu_{\max} > 2.1. \end{cases} \tag{8}$$

Similarly, $\log \sigma_g$ exhibits an approximately linear dependence on $\log \nu_{\max}$, but with a mild deviation from strict linearity. To capture this trend more accurately, we fitted the relation between $\log \sigma_g$ and $\log \nu_{\max}$ using a fourth-order polynomial. The coefficients from higher-order terms to lower-order terms are 0.142 ± 0.011, -1.00 ± 0.085, 2.476 ± 0.243, -1.697 ± 0.299, and 0.451 ± 0.133, respectively. The resulting fit is shown as the blue solid line in Figure 4(b).

We also evaluated the goodness of fit in the vicinity of the excess power hump, defined as the frequency range from $\nu_{\max} - 3\sigma_g$ to $\nu_{\max} + 3\sigma_g$. The formula for calculating the goodness of fit is as follows:

$$R^2 = 1 - \frac{\sum_i (y_i - \hat{y}_i)^2}{\sum_i (y_i - \bar{y})^2}, \tag{9}$$

where y_i represents the observed values, $\hat{y}_i$ denotes the fitted value from the model, and $\bar{y}$ is the mean of the observed values. The distribution of the goodness of fit as a function of $\nu_{\max}$ is shown in Figure 4(c). Although the fitting was performed in logarithmic space, the goodness of fit was evaluated in linear space. As illustrated in Figure 4(c), the majority of the excess power humps are well reproduced, indicating that performing the fitting in logarithmic space is justified.

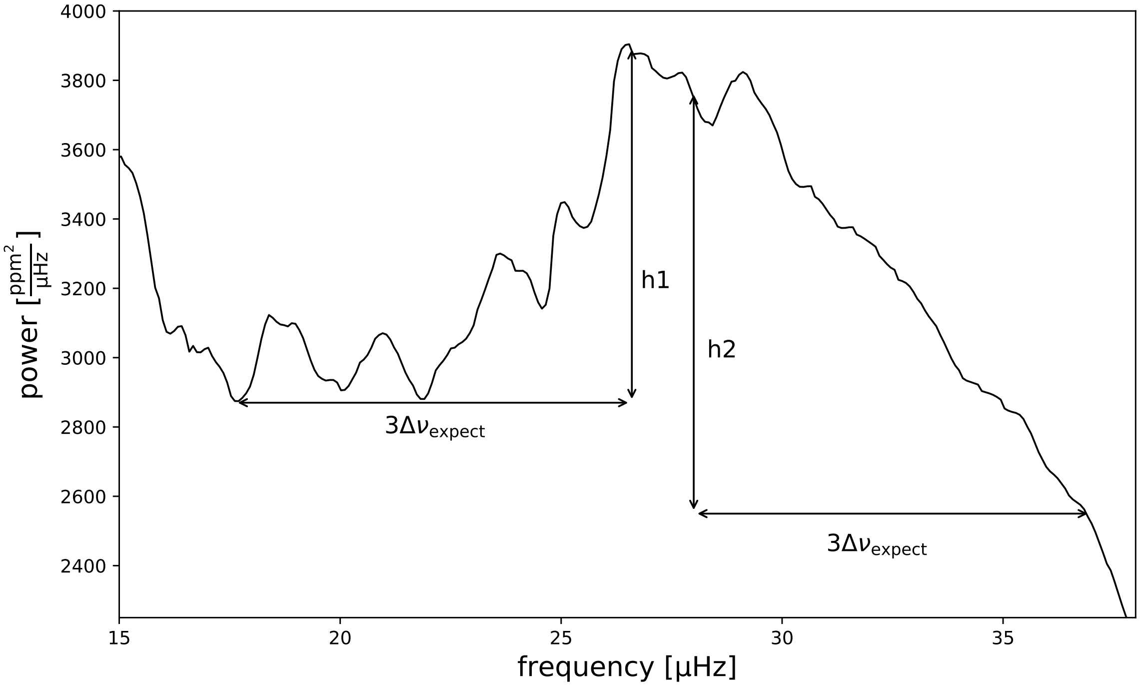

Figure 5. Smoothed PSD of TIC 469248308, where h_1 and h_2 must satisfy Equations (10) and (11), respectively, in order to be considered a potential solar-like oscillation.

4.3. Search for Oscillations

In the absence of oscillations or other distinctive signals, the underlying trend of the PSD either decreases or remains flat with increasing frequency, implying a trend slope $\leqslant 0$. The excess power hump of solar-like oscillations produces a localized positive slope in this trend. We therefore aim to detect the excess power hump by identifying such changes in the slope of the trend of the PSD. Obtaining the underlying trend of a curve by applying a boxcar mean is a common practice. However, since solar-like oscillations with different $\nu_{\max}$ values possess different $\Delta\nu$, extracting the trend near the hump requires a smoothing scale that depends on $\Delta\nu$. Therefore, our method applies a running mean with a variable window of $4\Delta\nu_{\odot}\cdot(\nu/\nu_{\max,\odot})^{0.784}$ (denoted $\Delta\nu_{\mathrm{expect}}$) to the PSD, where ν denotes frequency.

Random fluctuations in the smoothed curve, whose amplitude depends on the smoothing window size, prevent the direct detection of the excess power hump from the slope. Therefore, we computed the slope of the smoothed PSD between points separated by $3\Delta\nu_{\mathrm{expect}}$, and defined a minimum slope threshold based on the smoothed high-frequency region (which only contains a white-noise component). The detailed procedure is outlined as follows. If $p(\nu)$ represents the smoothed PSD, we detect the excess power hump by verifying whether $p(\nu)$ satisfies the following two conditions (this process is illustrated in Figure 5):

$$p(\nu_1) - p(\nu_1 - 3\Delta\nu_{\mathrm{expect}}) \geqslant \text{threshold}, \tag{10}$$

and

$$p(\nu_2) - p(\nu_2 + 3\Delta\nu_{\mathrm{expect}}) \geqslant \text{threshold}, \tag{11}$$

where $\nu_1 \leqslant \nu_2$. The threshold was set to 3σ of the smoothed PSD above 3500 μHz, where the smoothing used a window size identical to that applied at ν_1. If ν_1 and ν_2 satisfying the above conditions are present in the smoothed PSD, we consider that the PSD may contain an excess power hump of solar-like oscillations.

Not all PSDs satisfying Equations (10) and (11) necessarily correspond to excess power humps from solar-like oscillations; some may arise from other signals or random fluctuations. To verify the nature of these features, we fitted each PSD using $(\nu_1 + \nu_2)/2$ as the initial $\nu_{\max}$, following the same procedure described in Section 4.2. We expect the fitted parameters D and σ_g of genuine solar-like oscillations to follow the distributions of those identified by Figure 4. Hence, PSDs with D and σ_g lying within 3σ of the fitted relations in Figures 4(a) and (b) (dashed lines) were classified as possible solar-like oscillators. Additionally, only fits with goodness-of-fit values exceeding the threshold indicated by the dashed line in Figure 4(c) were retained.

The method achieves a detection rate of about 91.5% and a false-positive rate of 2.7% when tested on 2749 oscillators identified by E. Hatt et al. (2023) in the southern ecliptic hemisphere and 2000 randomly selected stars from the same region (the detection rates in different $\nu_{\max}$ ranges are shown in Figure 6). Increasing the thresholds in Equations (10) and (11) to 4σ reduces the detection rate to 89.2% while lowering the false-positive rate to 1.8%.

The method was then applied to the light curves of all 220,000 sample stars, resulting in the identification of 16,800 candidates. Further visual inspection led to the identification of a final set of 10,548 solar-like oscillators. The distribution of these oscillators in the H-R diagram is shown in Figure 3.

5. Measuring $\nu_{\max}$ and $\Delta\nu$ with Autocorrelation

The segmented ACF of the spectrum method is employed to measure both $\nu_{\max}$ and $\Delta\nu$ (D. Huber et al. 2009). As described in Section 4.2, we fit an oscillation spectrum to obtain the $\nu_{\max,\mathrm{fit}}$ and then use Equation (6) to estimate $\Delta\nu$, denoted as $\Delta\nu_{\mathrm{estimate}}$. We then extract and analyze the

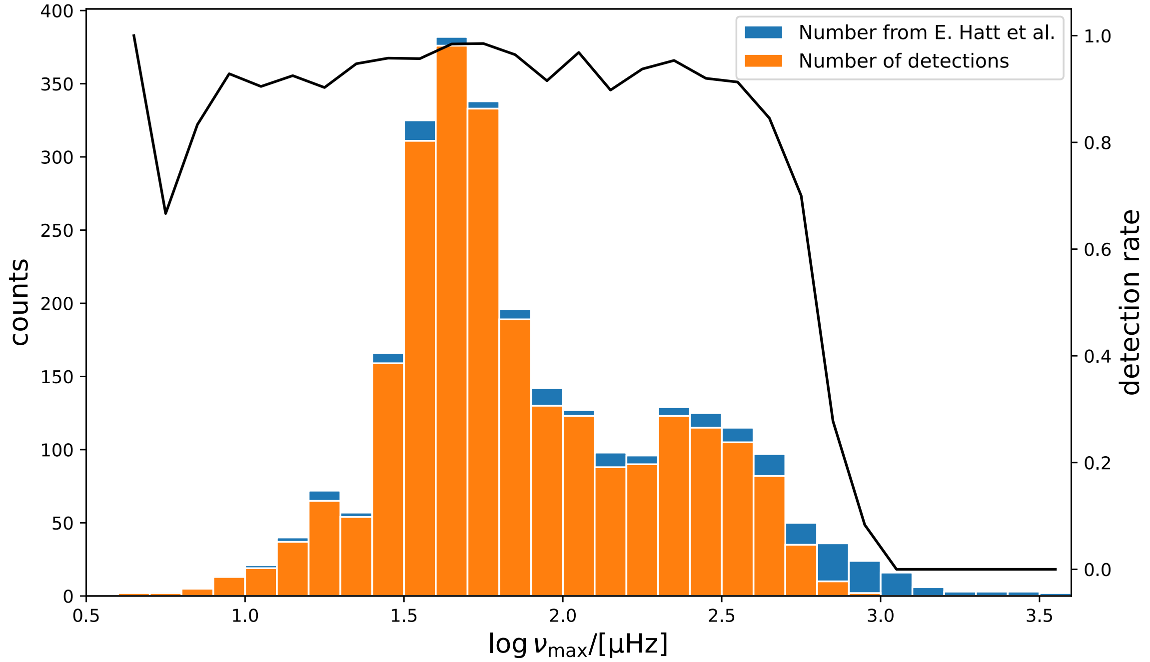

Figure 6. Detection rates in different $\nu_{\rm max}$ intervals. Blue bars denote the number of solar-like oscillators detected by E. Hatt et al. (2023), orange bars represent those recovered by our method, and the black line shows the detection rate as a function of $\nu_{\rm max}$.

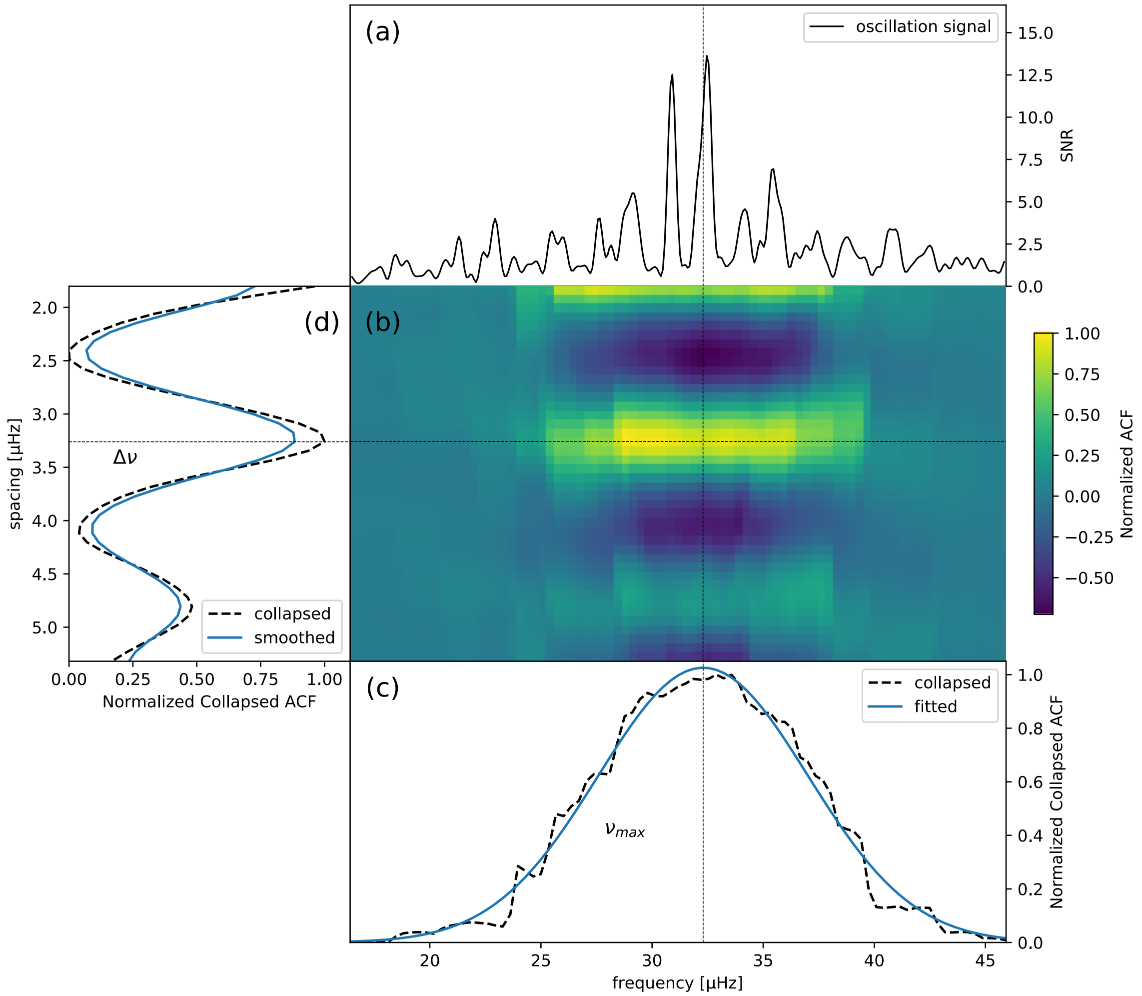

Figure 7. An example measurement of $\nu_{\rm max}$ and $\Delta\nu$ is shown for TIC 469248308. In panel (a), the black solid line represents the signal-to-noise ratio obtained by dividing the PSD by the background component. Panel (b) shows the ACF for all segments with each column along the vertical axis representing a subsegment ACF. Panels (c) and (d) display the results of panel (b) after vertical and horizontal collapsing, respectively. These results have been normalized, with the dashed lines indicating the measured values of $\nu_{\rm max}$ and $\Delta\nu$.

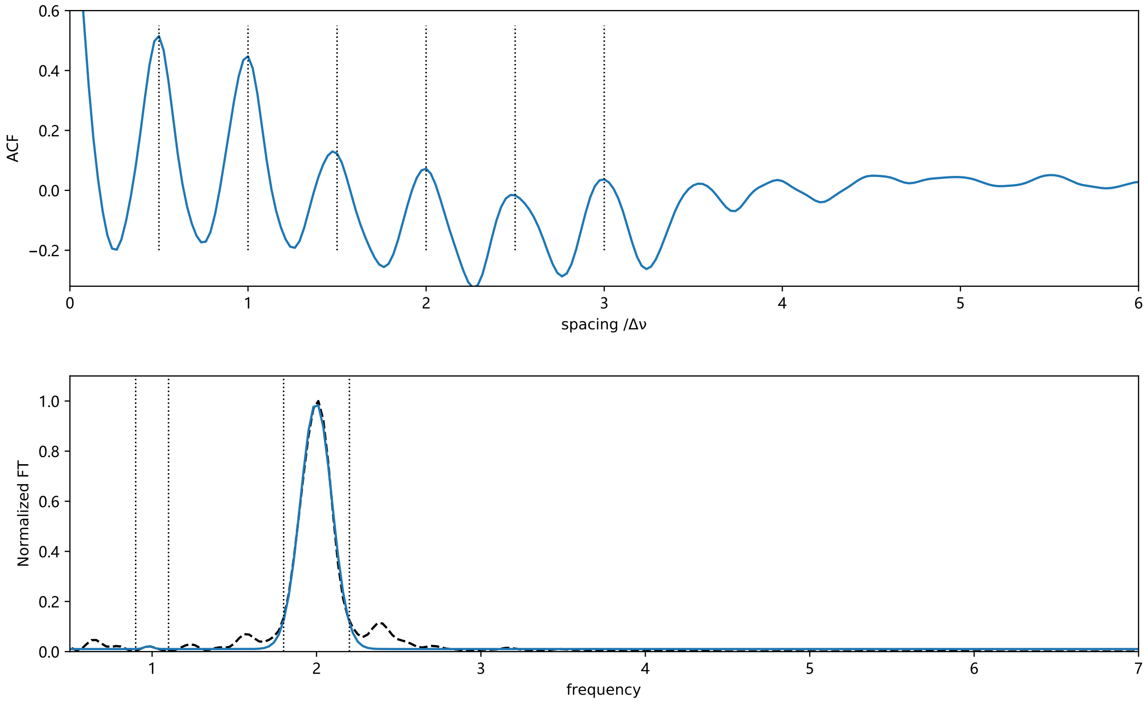

Figure 8. The upper panel displays the autocorrelation function (ACF) of the oscillations for TIC 469248308, and the lower panel shows the Fourier spectrum of the corresponding ACF. The black dashed line in the lower panel shows the normalized power spectrum, and the blue solid line represents its fit.

oscillation signal within the frequency range of $\nu_{\max,\mathrm{fit}} - 3\sigma_g - 2\Delta\nu_{\mathrm{estimate}}$ to $\nu_{\max,\mathrm{fit}} + 3\sigma_g + 2\Delta\nu_{\mathrm{estimate}}$. As shown in Figure 7, $\nu_{\max}$ and $\Delta\nu$ are measured.

As shown in Figure 7(a), we divided the original PSD by the background component. Next, the processed oscillations are divided into overlapping segments represented by their central frequency, each with a length of $4\Delta\nu_{\mathrm{estimate}}$ and a step of $0.1\Delta\nu_{\mathrm{estimate}}$. The ACF for each segment is calculated with spacing ranging from $0.5\Delta\nu_{\mathrm{estimate}}$ to $1.5\Delta\nu_{\mathrm{estimate}}$. This results in a two-dimensional matrix, as shown in Figure 7(b), where each column represents the ACF of a subsegment. Then, we collapse (normalizing after summing) the matrix and absolute values of the matrix along the horizontal and vertical axes, respectively. The collapsed results are presented in Figures 7(c) and (d). Subsequently, the collapsed result in Figure 7(c) is fitted with a Gaussian function. The value of $\nu_{\max}$ was adopted as the center of the fitted Gaussian function. The collapsed result in Figure 7(d) is Gaussian smoothed with $\sigma = 0.05\Delta\nu_{\mathrm{estimate}}$ and the measurement of $\Delta\nu$ was taken as the maximum peak in the range of $0.7\Delta\nu_{\mathrm{estimate}}$ to $1.3\Delta\nu_{\mathrm{estimate}}$.

Following the approach of D. Huber et al. (2011), we perturb the power spectrum using a χ^2 distribution with 2 degrees of freedom and recompute $\nu_{\max}$ and $\Delta\nu$ for each realization. After 500 iterations, the standard deviations of the resulting distributions are adopted as the uncertainties in $\nu_{\max}$ and $\Delta\nu$.

The above method for calculating $\Delta\nu$ always returns a value, but not all solar-like oscillators yield a reliable $\Delta\nu$. Therefore, we assessed the reliability of $\Delta\nu$ using the discrete Fourier transform of the ACF of the oscillation signal (J. Zhou et al. 2024). According to the asymptotic representation of high-order p-modes (C. Aerts 2021),

$$\nu_{nl} \simeq \left(n + \frac{l}{2} + \frac{1}{4} + \alpha\right)\Delta\nu, \tag{12}$$

the ACF of solar-like oscillations exhibits regularly spaced peaks, located at half-integer multiples of the large frequency spacing, as shown in Figure 8's upper panel (D. Huber et al. 2009). The quasiperiodic signal manifests as a distinct peak in the frequency domain. According to Parseval's theorem, the total energy of a signal is conserved between the time and frequency domains; therefore, the integrated power within a given frequency range reflects the energy associated with the corresponding periodicity. We thus quantify the reliability of $\Delta\nu$ as the ratio between the integrated power of the relevant peak in the power spectrum of ACF and the total integrated power. The procedure is as follows. First, we compute the ACF of the solar-like oscillation signal (Figure 7(a)) and normalize its horizontal axis by dividing by $\Delta\nu$ (Figure 8). We then remove the long-period trend in the ACF by performing a linear fit and compute the power spectrum for spacings greater than 0.2 using a Fourier transform. Subsequently, we identify the highest peaks in the ranges 0.9–1.1 and 1.8–2.2, fit them with two Gaussian functions, and finally calculate the ratio of the integrated power within 2σ of the fitted Gaussians to the total integrated power.

We analyzed 2694 solar-like oscillators identified by E. Hatt et al. (2023). Only those stars whose $\Delta\nu$ values agree with the literature within 10% were considered reliable measurements, resulting in a total of 2375 stars meeting this criterion. For these stars, we calculated the ratio as described above (blue points in Figure 9). To construct a reference sample representing noise backgrounds, we randomly selected 2694 stars from the sample of 220,000 stars excluding oscillators and fitted their PSDs using a Harvey model without a Gaussian

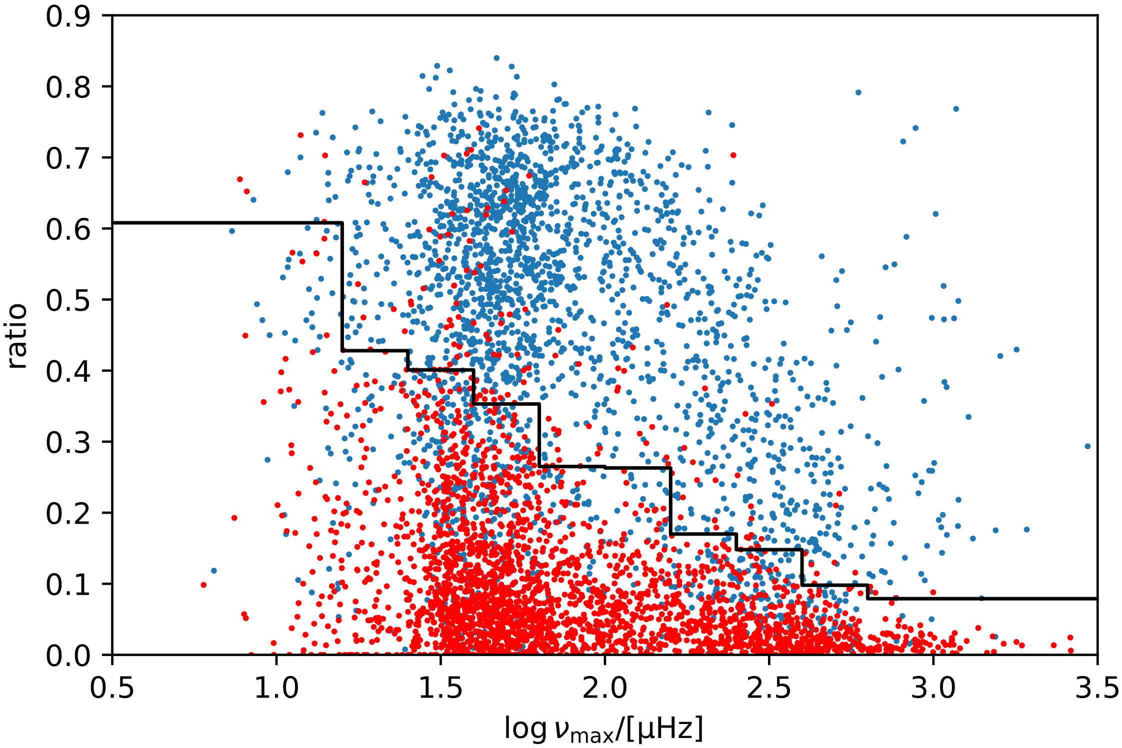

Figure 9. Blue dots represent the ratios (as described in Section 5) of oscillating stars from the literature, while red dots indicate the ratios of nonoscillating stars. The black solid line denotes the 95th percentile of the ratio distribution for nonoscillating stars.

Table 1
Stellar Global Oscillation Parameters

TIC (1)	$T_{\rm eff}$ (K) (2)	rad ($R_\odot$) (3)	[Fe/H] (4)	$\log g$ (5)	$\nu_{\rm max,fit}$ (μHz) (6)	$\nu_{\rm max}$ (μHz) (7)	$\Delta\nu$ (μHz) (8)	$N_{\rm sectors}$ (9)
				Type 1				
1608	4799	12.191	−0.0544	2.677	45.01 ± 0.92	47.98 ± 1.77	4.72 ± 0.19	2
13727	5216	3.960	…	…	187.97 ± 1.34	190.13 ± 2.17	15.87 ± 0.23	2
70380	4991	10.247	…	…	38.50 ± 2.43	41.21 ± 1.52	4.46 ± 0.55	3
80047	4814	6.537	0.0382	2.932	68.02 ± 1.40	70.83 ± 2.64	6.95 ± 0.18	1
89696	4892	8.302	−0.0323	3.015	43.00 ± 0.36	43.29 ± 0.57	4.89 ± 0.55	1
105245	4879	3.979	−0.0617	3.342	274.17 ± 3.1	272.56 ± 2.29	18.53 ± 0.44	3
589906	4305	15.999	…	…	16.41 ± 0.32	16.77 ± 0.48	2.06 ± 0.09	2
608932	4945	8.908	−0.1266	2.842	60.90 ± 1.17	61.73 ± 1.51	5.41 ± 0.32	1
612908	4895	5.003	−0.2288	3.196	167.11 ± 1.48	166.39 ± 1.51	13.47 ± 0.21	2
770660	5102	10.749	−0.0399	2.872	63.14 ± 2.68	65.61 ± 2.62	6.01 ± 0.41	2
				Type 2				
11001	4510	15.606	…	…	17.13 ± 0.63	18.55 ± 0.74	…	2
74676	4340	…	…	…	16.98 ± 0.38	17.10 ± 0.62	…	3
92094	4728	10.823	0.1524	2.698	43.01 ± 0.68	46.15 ± 1.41	…	3
111876	4572	11.330	0.2021	2.556	38.13 ± 0.79	38.63 ± 1.07	…	3
148113	4348	20.721	…	…	10.87 ± 1.88	12.77 ± 0.99	…	2
152762	4785	10.826	…	…	36.78 ± 0.42	39.25 ± 0.97	…	3
155455	4423	22.478	…	…	13.91 ± 0.20	13.84 ± 0.17	…	4
627296	4668	11.020	…	…	29.70 ± 0.67	31.45 ± 1.39	…	2
683071	4782	10.822	…	…	34.65 ± 0.55	36.26 ± 1.09	…	2
710187	4920	9.339	−0.0268	2.903	83.17 ± 1.24	87.81 ± 2.22	…	2

Note. The data presented in the table is sourced from the TESS Input Catalog, including $T_{\rm eff}$ and radii; [Fe/H] and $\log g$ are sourced from Gaia.

envelope. For each of these stars, we estimated the signal-to-noise ratio and then injected the $\nu_{\rm max}$ and σ_g values derived from the corresponding real oscillators to define the same frequency range used in the $\Delta\nu$ measurement. These frequency segments were subsequently processed through the same $\Delta\nu$ measuring, yielding a spurious "$\Delta\nu$" for each

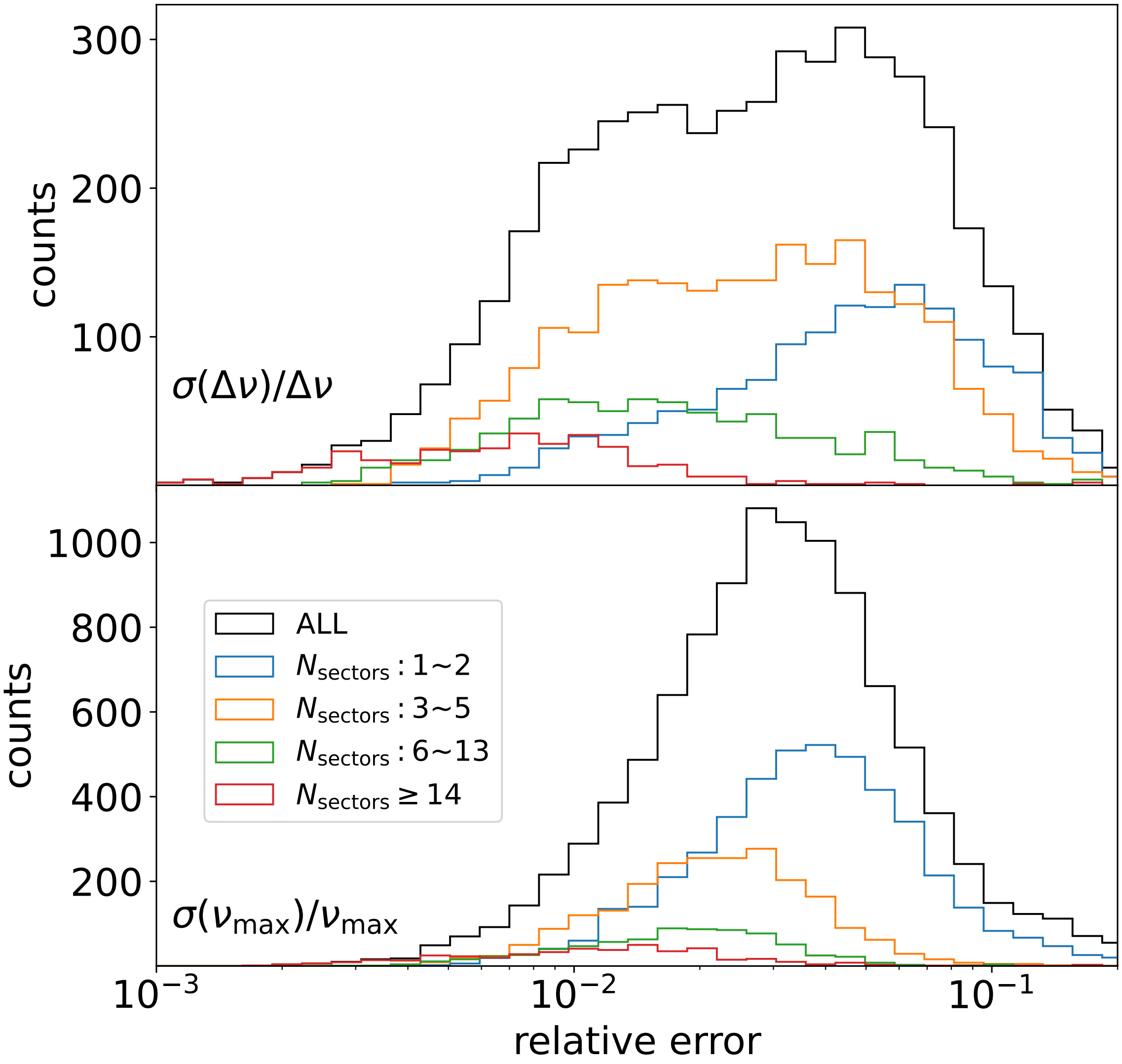

Figure 10. The upper and lower panels present the uncertainty distributions of $\Delta\nu$ and $\nu_{\rm max}$, respectively. $N_{\rm sectors}$ indicates the number of observing sectors.

background star. Finally, we computed the ratio as described above (red points in Figure 9), to characterize the apparent periodicity in the noise sample.

As shown in Figure 9, although oscillating and nonoscillating stars cannot be fully separated, their ratio distributions differ markedly. The black solid line indicates the 95th percentile of the ratio distribution for nonoscillating stars. Using this line as the threshold, 1788 of the 2375 oscillators lie above it, while 587 fall below it. Oscillators identified in this work above this line are classified as Type 1 ($\Delta\nu$ are considered reliable), while those below are classified as Type 2 ($\Delta\nu$ are considered unreliable). Among the 10,548 oscillating stars identified, 4775 are labeled as Type 1 and 5773 as Type 2. The results of the measurements are listed in Table 1.

The distributions of the $\Delta\nu$ uncertainties for the Type 1 oscillators and the $\nu_{\rm max}$ uncertainties for all oscillators are shown in Figure 10. The curves in different colors represent the uncertainty distributions for stars observed in different numbers of TESS sectors. As shown in the figure, the measurement uncertainties decrease with increasing observing time, a trend that is consistent with the results reported by J. Zhou et al. (2024).

6. Result

6.1. Comparison with Fundamental Stellar Parameters

According to Equation (4), stellar radii can be estimated from the solar-like oscillation parameters $\nu_{\rm max}$, $\Delta\nu$, and the effective temperature (where we adopt $f_{\Delta\nu} = 1$ and $f_{\nu_{\rm max}} = 1$). Since the TESS Input Catalog (TIC; K. G. Stassun et al. 2018, 2019) also provides $T_{\rm eff}$ and stellar radii, we use these catalog values as an external reference to verify search results in this work. For stars classified as Type 2, their $\Delta\nu$ values are estimated using Equation (6). The comparison between the asteroseismic radii $R_{\rm seis}$ and the TIC radii R is presented in Figure 11. The lower panel shows the fractional residuals between the $R_{\rm seis}$ and the R. For stars classified as Type 1 (left panels), the median, 5th percentile, and 95th percentile of the fractional residuals (indicated by the dashed and dotted lines) are 9.6%, −6.9%, and 32.2%, respectively. For Type 2 stars (right panels), these values are 7.3%, −21.9%, and 42.9%, respectively.

For the Type 1 stars, a clear systematic offset is visible. This discrepancy is likely due to the lack of a correction factor in the asteroseismic radius calculation. Figure 7 of S. Sharma et al. (2016) provides the correction factor $f_{\Delta\nu}$, which depends

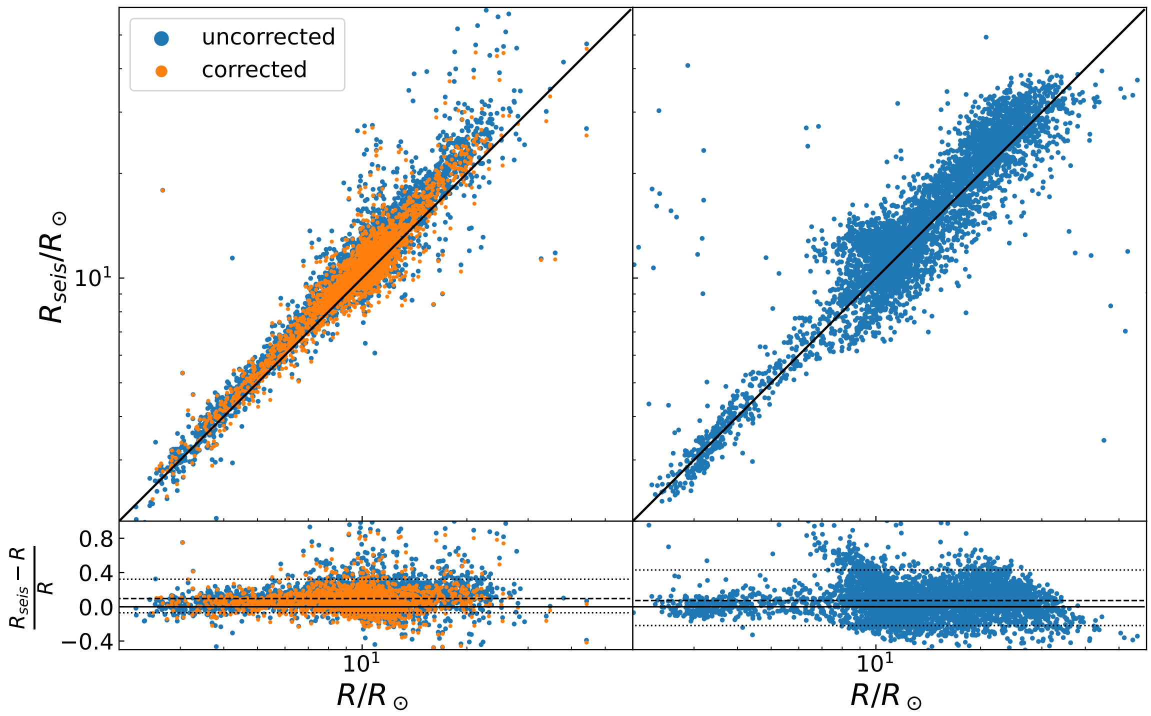

Figure 11. $R_{\rm photo}$ versus $R_{\rm seis}$: comparison of radii calculated from the scaling relation and from the TESS Input Catalog. The left panels show the oscillators classified as Type 1, and the right panels show those classified as Type 2. In the upper panels, the solid lines indicate the 1:1 equality line. The lower panels display the fractional residuals between the two calculated radii. The dashed lines denote the median of the fractional residuals, while the dotted lines indicate the 5th percentile and 95th percentile of the fractional residuals.

on [Fe/H], mass, and evolutionary state. By crossmatching with Gaia, we obtained [Fe/H] and mass for 2449 Type 1 oscillators. However, we were unable to distinguish between the pre-RGB-tip and post-RGB-tip evolutionary phases. Since all oscillators in this work have an effective temperatures above 4000 K, and the correction factor for post-RGB-tip stars at $T_{\rm eff} > 4000$ K is close to unity 1.0, we adopted the pre-RGB-tip correction for all 2449 stars. The corrected radii are shown as orange points in Figure 10. After applying the correction, the median fractional residual decreases to 5.8%. However, a systematic offset still remains, suggesting that additional corrections, such as for $\nu_{\rm max}$, may be necessary.

We also compared the surface gravity derived from Gaia DR3 with that obtained from scaling relations. We used TOPCAT[14] to crossmatch positional coordinates within a $1''$ radius to obtain stellar parameters from Gaia DR3. As a result of the crossmatch, we obtained 9666 oscillators, of which only 5191 have surface gravity $\log g_{\rm Gaia}$ (from GSP-Phot). The surface gravity $\log g_{\rm seis}$ can be also calculated using Equation (5). The comparison between the $\log g_{\rm seis}$ and the $\log g_{\rm Gaia}$ is presented in Figure 12. The lower panel shows the residuals between $\log g_{\rm Gaia}$ and $\log g_{\rm seis}$. For oscillators classified as Type 1 (left panels) the median, 5th percentile, and 95th percentile of the residuals are 0.068, −0.289, and 0.370, respectively. For Type 2 stars (right panels), these values are 0.151, −0.256, and 0.550, respectively. Additionally, as shown in lower panels of Figure 12, a systematic bias is observed between $\log g_{\rm Gaia}$ and $\log g_{\rm seis}$, with $\log g_{\rm Gaia}$ slightly higher than $\log g_{\rm seis}$ at lower $\log g$ values. This is consistent with Figure 10 in R. Andrae et al. (2023).

6.2. Comparison with the Literature

As shown in Figure 13, we compare the distribution of oscillators identified in this work with those reported in previous studies (M. Hon et al. 2021, 2022; E. Hatt et al. 2023; J. Zhou et al. 2024) as a function of $\nu_{\rm max}$. In the TESS 2 minute cadence targets of the southern ecliptic hemisphere, this work yields the largest number of detected oscillators among all studies. In addition, this work contributes 2972 newly identified oscillators that were not reported in the earlier literature, of which 717 are classified as Type 1. More than half of the new detections fall within the frequency regime of $\nu_{\rm max} < 20\ \mu$Hz. Among the Type 1 oscillators, 1920 were not provided with $\Delta\nu$ measurements in previous studies.

We compared the asteroseismic parameters derived in this work with those reported in the literature. Figure 14 shows the $\nu_{\rm max}$ values for the oscillators common to both samples, with the lower panel presenting the fractional residuals between the literature values and our measurements. The median, 5th percentile, and 95th percentile of fractional residuals are −1.9%, −12.4% and 9.7%, respectively. Figure 15 shows the comparison of $\Delta\nu$ for the Type 1 oscillators. The fractional residuals have a median of 0.8%, with the 5th and 95th percentiles at −5.7% and 7.8%, respectively.

We assessed the consistency between the parameters measured in this work and those reported in previous studies using the inequality $|{\rm Para}_{\rm this\ work} - {\rm Para}_{\rm literature}| \leqslant ({\rm error}^2_{\rm this\ work} + {\rm error}^2_{\rm literature})^{1/2}$, where Para represents either $\Delta\nu$ or $\nu_{\rm max}$. For $\Delta\nu$, among oscillators for which $\Delta\nu$ values are available both in this work and in M. Hon et al. (2022), E. Hatt et al. (2023), and J. Zhou et al. (2024), the fractions satisfying this inequality are 48%, 64%, and 82%, respectively. For $\nu_{\rm max}$, among oscillators in common between this work and

---

[14] https://www.star.bris.ac.uk/~mbt/topcat

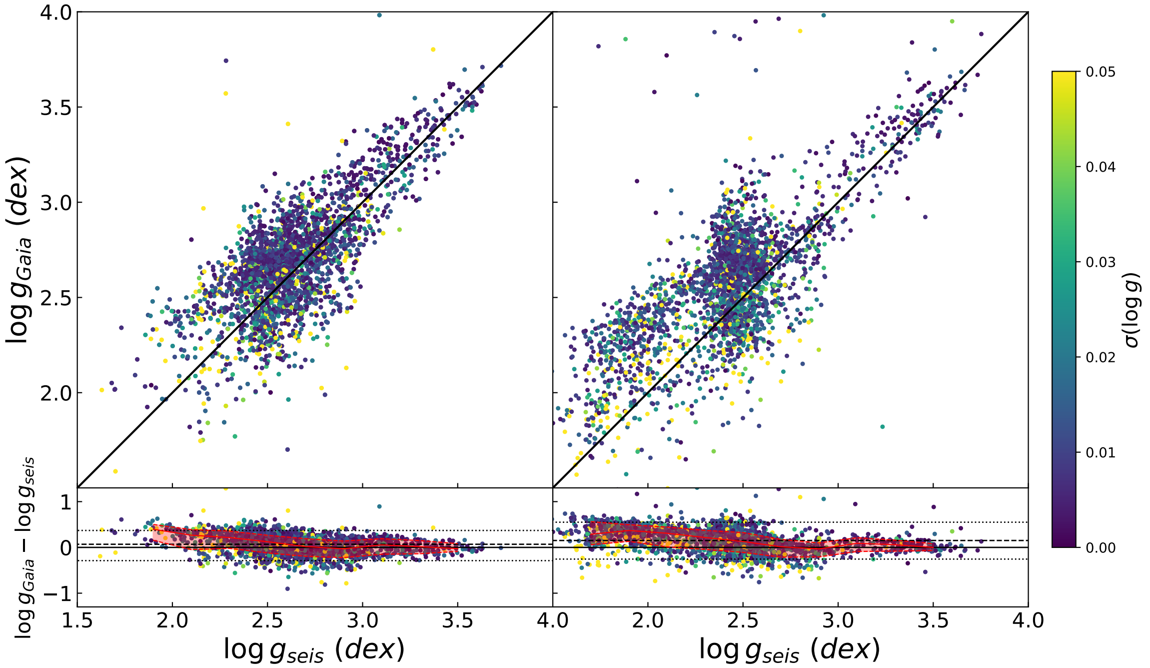

Figure 12. $\log g_{\mathrm{Gaia}}$ versus $\log g_{\mathrm{seis}}$: a comparison of surface gravity $\log g$ derived from scaling relations and Gaia DR3 data. In the upper panels, the solid lines represent the 1:1 equality line, and the color bar represents the error of $\log g_{\mathrm{Gaia}}$. The lower panels display the residuals of $\log g_{\mathrm{Gaia}} - \log g_{\mathrm{seis}}$. The red shaded area marks the region encompassing 68% of the data within bins of width 0.2.

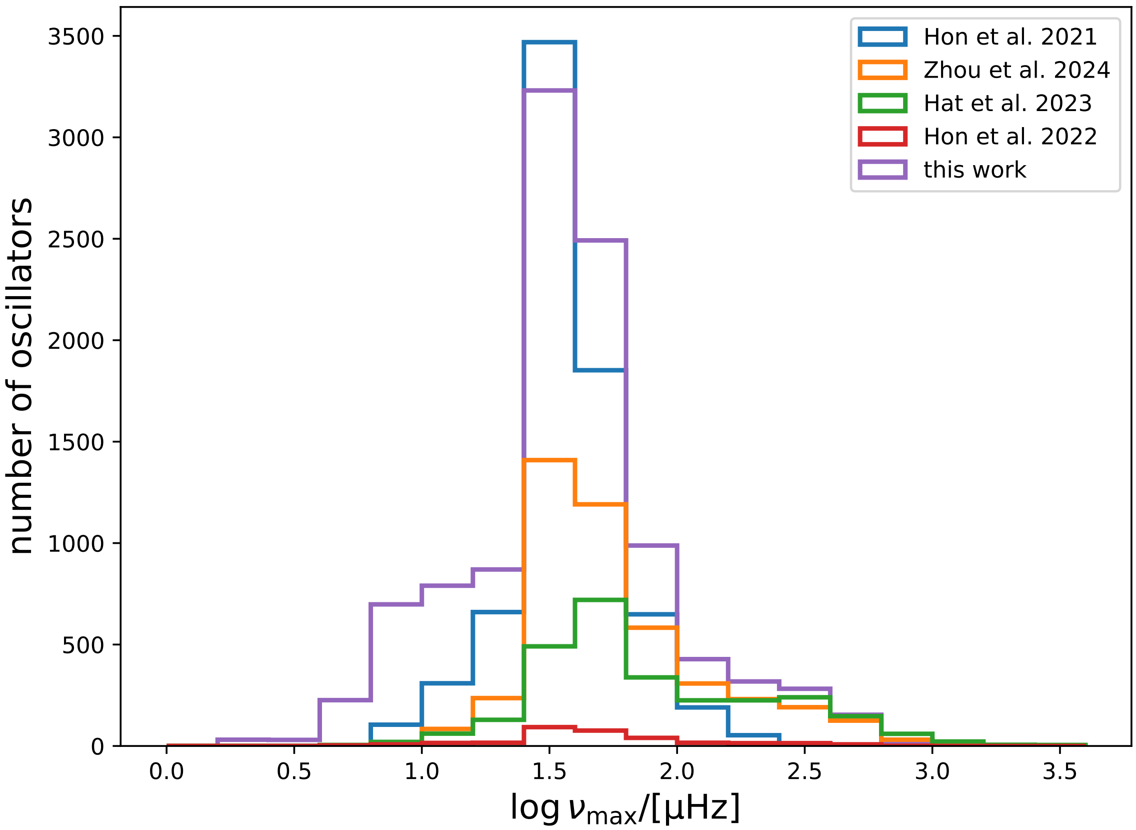

Figure 13. Comparison between the number of oscillators reported in the literature and those detected in this work within the 220,000 target stars analyzed.

M. Hon et al. (2021, 2022), E. Hatt et al. (2023), and J. Zhou et al. (2024), the corresponding fractions are 77%, 37%, 50%, and 75%, respectively. Overall, the parameters derived in this work show good agreement with those reported in most previous studies, except for a relatively poorer consistency with the $\nu_{\max}$ values from E. Hatt et al. (2023) and with the parameters from M. Hon et al. (2021). As shown in Figures 14 and 15, although the differences between the parameters from M. Hon et al. (2021) and those obtained in this work are not large, the consistency metric yields poor

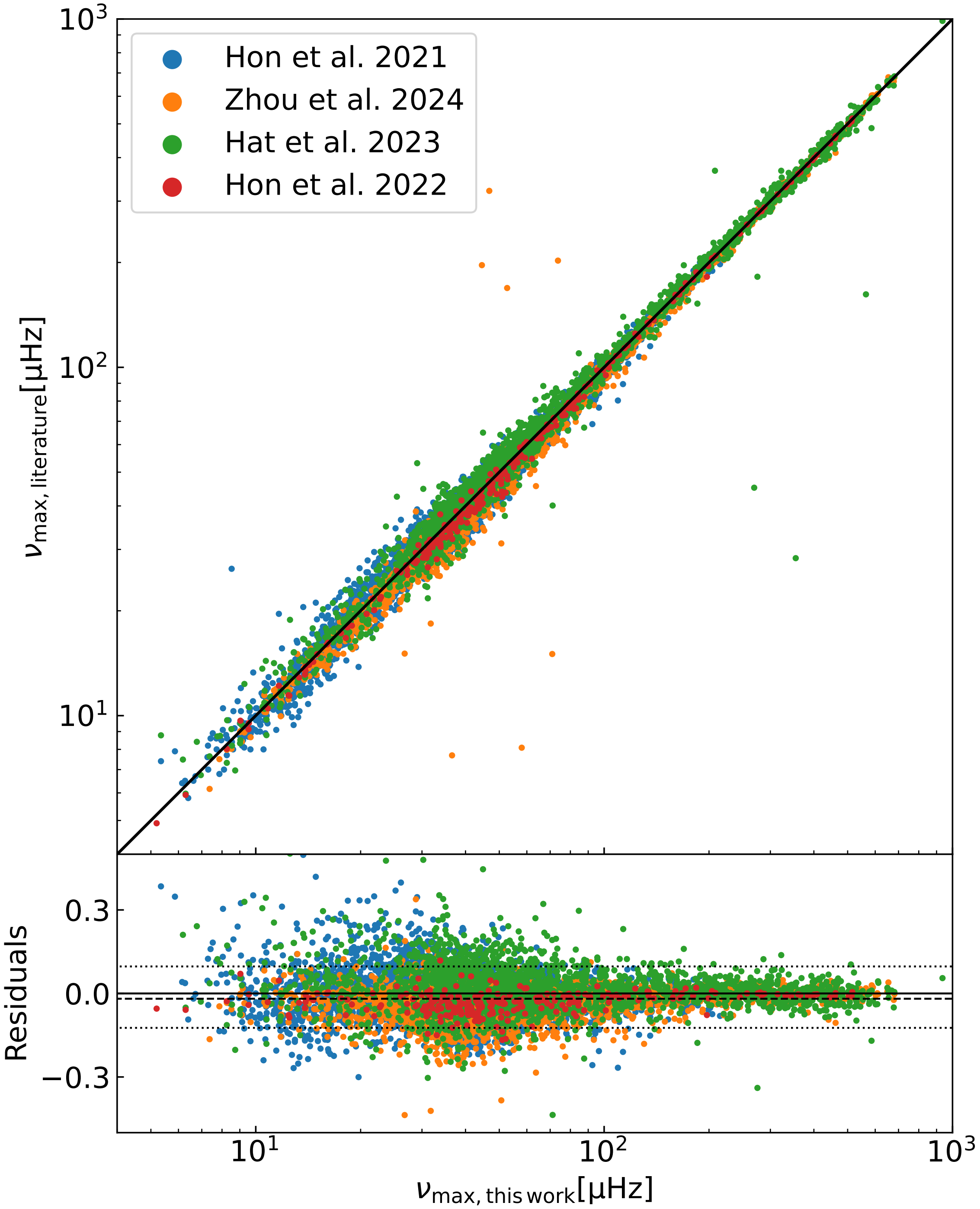

Figure 14. Comparison between the $\nu_{\max}$ values reported in the literature and those measured in this work. The lower panels display fractional residuals between $\nu_{\max}$ values, calculated as $(\nu_{\mathrm{max,literature}} - \nu_{\mathrm{max,this\ work}})/\nu_{\mathrm{max,this\ work}}$. The dashed lines denote the median of the fractional residuals, while the dotted lines indicate the 5th percentile and 95th percentile of the fractional residuals.

consistency. This may be attributed to the fact that stars observed in continuous viewing zones of TESS benefit from longer effective observing times, leading to smaller formal uncertainties. In such cases, the estimation of uncertainties may require additional consideration of the frequency resolution.

7. Summary

In this work, we present a novel method searching for solar-like oscillators. The method detects excess power humps by examining the slope of the PSD profile and by applying selection criteria derived from fitting the oscillation spectra of known solar-like oscillators from E. Hatt et al. (2023). Applying this method to the 220,000 TESS 2 minute targets in the southern ecliptic hemisphere yielded 16,800 candidates. After visual inspection, we identified 10,548 solar-like oscillators. We measured $\nu_{\max}$ and $\Delta\nu$ using the segmented autocorrelation technique, and assessed the reliability of the $\Delta\nu$ measurements through the Fourier transform of the ACF. Based on this assessment, 4775 oscillators were classified as Type 1 (reliable $\Delta\nu$) and 5773 as Type 2 (unreliable $\Delta\nu$). We compared the asteroseismic radii and surface gravities derived

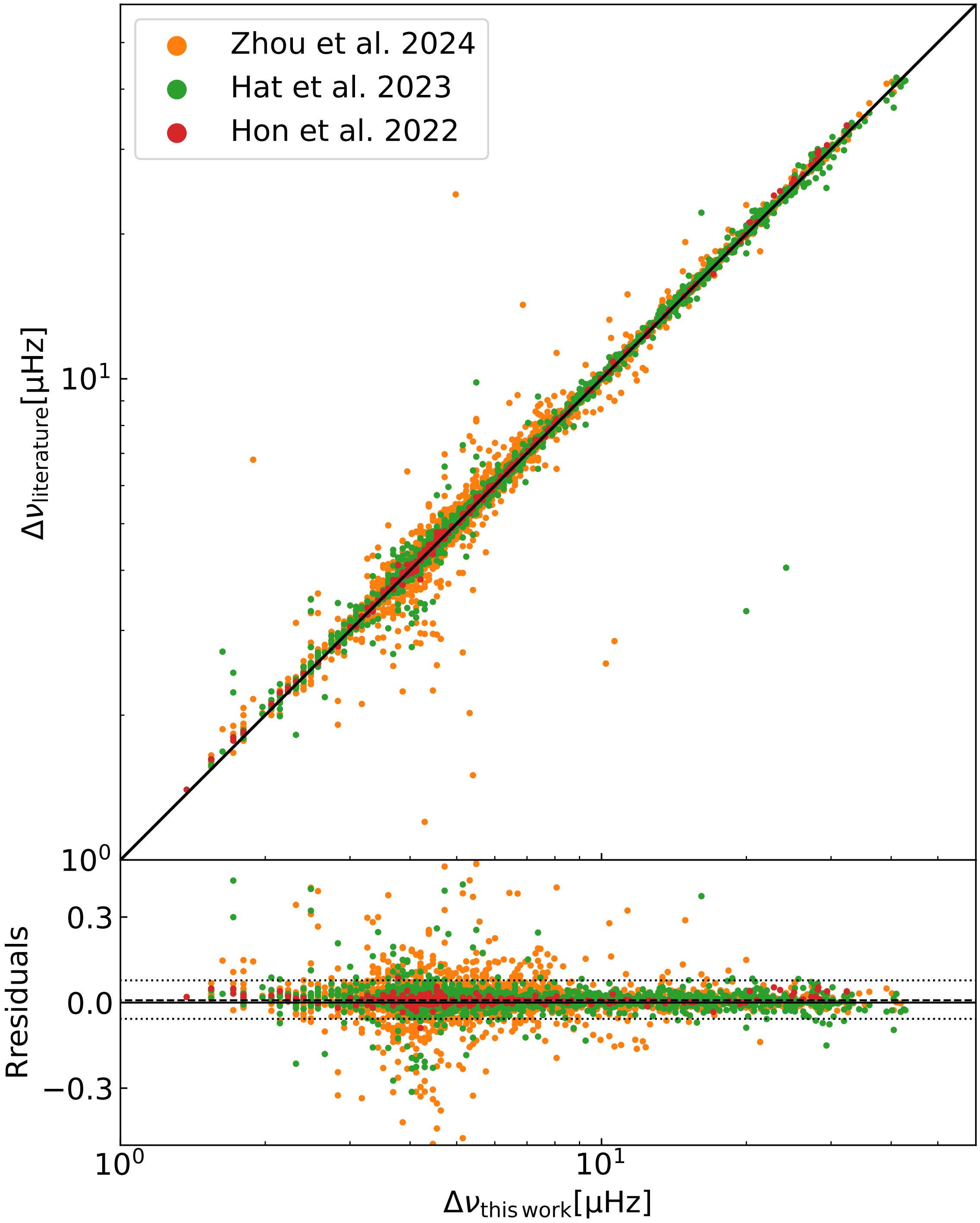

Figure 15. Comparison between the $\Delta\nu$ values reported in the literature and those measured in this work for oscillators classified as Type 1. The lower panels display the fractional residuals of $\Delta\nu$, calculated as $(\Delta\nu_{\rm literature} - \Delta\nu_{\rm this\ work})/\Delta\nu_{\rm this\ work}$. The dashed lines denote the median of the fractional residuals, while the dotted lines indicate the 5th percentile and 95th percentile of the fractional residuals.

from the scaling relations with the radii from the TIC and the $\log g$ values from Gaia DR3. A systematic offset is found between the asteroseismic radii and those listed in the TIC. After applying the $\Delta\nu$ correction factor of S. Sharma et al. (2016), the median fractional residual decreases from 9.6% to 5.8%, although a systematic difference remains, suggesting that additional corrections may be required. Compared with previous studies, this work adds 2972 newly identified TESS oscillators, including 717 high-quality stars classified as Type 1. In addition, the Type 1 sample contains 1920 oscillators for which no $\Delta\nu$ measurements were provided in earlier studies. Finally, the $\nu_{\rm max}$ and $\Delta\nu$ values derived in this study show good agreement with literature measurements, confirming the reliability of the asteroseismic parameters obtained here.

Acknowledgments

This work is cosupported by the National Natural Science Foundation of China (grant No. 12288102), the National Key R&D Program of China (grant No. 2021YFA1600400/

2021YFA1600402), and the B-type Strategic Priority Program of the Chinese Academy of Sciences (grant No. XDB1160202/XDB41000000). The authors also gratefully acknowledge the support from the NSFC of China (grant Nos. 12133011 and 12273104), Yunnan Fundamental Research Projects (grant No. 202401AS070045), the Youth Innovation Promotion Association of Chinese Academy of Sciences, the Ten Thousand Talents Program of Yunnan for Top-notch Young Talents, the China Manned Space Program (grant No. CMS-CSST-2025-A14/CMS-CSST-2025-A01), and the International Centre of Supernovae (ICESUN), Yunnan Key Laboratory of Supernova Research (grant No. 202505AV340004). H.-F.X. acknowledges support from the National Natural Science Foundation of China (NSFC; No. 12303036) and the Scientific and Technological Innovation Programs of Higher Education Institutions in Shanxi (STIP; 2025Q032). This work utilized open data from the Transiting Exoplanet Survey Satellite (TESS) mission and the Gaia mission. The TESS data were provided by NASA and can be accessed via the MAST archive (https://archive.stsci.edu/), while the Gaia data were made available by the European Space Agency (ESA) and are publicly accessible through the Gaia archive (https://www.cosmos.esa.int/web/gaia). The authors gratefully acknowledge the use of Python and several open-source Python packages, including NumPy (C. R. Harris et al. 2020), SciPy (P. Virtanen et al. 2020), Matplotlib (J. D. Hunter 2007), Astropy (Astropy Collaboration et al. 2022), Pandas (W. McKinney 2010) and lightkurve (Lightkurve Collaboration et al. 2018), which were crucial for data processing, analysis, and visualization. Additionally, the authors thank the developers of TOPCAT (M. B. Taylor 2005), which was used for performing positional crossmatching of stars in this work. The authors would like to thank ChatGPT, an AI language model developed by OpenAI, for providing assistance with writing, editing, and improving the clarity of the manuscript.

ORCID iDs

Tao Wu https://orcid.org/0000-0001-6832-4325
Hui-Fang Xue https://orcid.org/0000-0001-6027-4562
Jia-Shu Niu https://orcid.org/0000-0001-5232-9500

References

Aerts, C. 2021, RvMP, 93, 015001
Andrae, R., Fouesneau, M., Sordo, R., et al. 2023, A&A, 674, A27
Astropy Collaboration, Price-Whelan, A. M., Lim, P. L., et al. 2022, ApJ, 935, 167
Baglin, A., Auvergne, M., Boisnard, L., et al. 2006, in 36th COSPAR Scientific Assembly, 3749
Bedding, T. R., & Kjeldsen, H. 2022, RNAAS, 6, 202
Bellinger, E. P. 2019, MNRAS, 486, 4612
Bellinger, E. P., Hekker, S., Angelou, G. C., Stokholm, A., & Basu, S. 2019, A&A, 622, A130
Borucki, W. J., Koch, D., Basri, G., et al. 2010, Sci, 327, 977
Ginsburg, A., Sipőcz, B. M., Brasseur, C. E., et al. 2019, AJ, 157, 98
Harris, C. R., Millman, K. J., van der Walt, S. J., et al. 2020, Natur, 585, 357
Harvey, J. 1985, ESASP, 235, 199
Hatt, E., Nielsen, M. B., Chaplin, W. J., et al. 2023, A&A, 669, A67
Hekker, S. 2020, FrASS, 7, 3
Hekker, S., Gilliland, R. L., Elsworth, Y., et al. 2011, MNRAS, 414, 2594
Hekker, S., Kallinger, T., Baudin, F., et al. 2009, A&A, 506, 465
Hon, M., Huber, D., Kuszlewicz, J. S., et al. 2021, ApJ, 919, 131
Hon, M., Kuszlewicz, J. S., Huber, D., Stello, D., & Reyes, C. 2022, AJ, 164, 135
Howell, S. B., Sobeck, C., Haas, M., et al. 2014, PASP, 126, 398
Huber, D., Bedding, T. R., Stello, D., et al. 2011, ApJ, 743, 143
Huber, D., Silva Aguirre, V., Matthews, J. M., et al. 2014, ApJS, 211, 2
Huber, D., Stello, D., Bedding, T. R., et al. 2009, CoAst, 160, 74
Hunter, J. D. 2007, CSE, 9, 90
Jiang, C., Jiang, B. W., Christensen-Dalsgaard, J., et al. 2011, ApJ, 742, 120
Joshi, S., & Joshi, Y. C. 2015, JApA, 36, 33
Kallinger, T., Mosser, B., Hekker, S., et al. 2010a, A&A, 522, A1
Kallinger, T., Weiss, W. W., Barban, C., et al. 2010b, A&A, 509, A77
Kjeldsen, H., & Bedding, T. R. 1995, A&A, 293, 87
Li, T., Li, Y., Bi, S., et al. 2022, ApJ, 927, 167
Lightkurve Collaboration, Cardoso, J. V. d. M., Hedges, C., et al. 2018, Lightkurve: Kepler and TESS time series analysis in Python, Astrophysics Source Code Library, ascl:1812.013
Lomb, N. R. 1976, Ap&SS, 39, 447
Mathur, S., García, R. A., Huber, D., et al. 2016, ApJ, 827, 50
McKinney, W. 2010, in Proc. of the 9th Python in Science Conf., ed. S. van der Walt & J. Millman (SciPy), 56
Mosser, B., Belkacem, K., Goupil, M. J., et al. 2010, A&A, 517, A22
Nielsen, M. B., Hatt, E., Chaplin, W. J., Ball, W. H., & Davies, G. R. 2022, A&A, 663, A51
Ricker, G. R., Winn, J. N., Vanderspek, R., et al. 2015, JATIS, 1, 014003
Scargle, J. D. 1982, ApJ, 263, 835
Sharma, S., Stello, D., Bland-Hawthorn, J., Huber, D., & Bedding, T. R. 2016, ApJ, 822, 15
Silva Aguirre, V., Stello, D., Stokholm, A., et al. 2020, ApJL, 889, L34
Stassun, K. G., Oelkers, R. J., Paegert, M., et al. 2019, AJ, 158, 138
Stassun, K. G., Oelkers, R. J., Pepper, J., et al. 2018, AJ, 156, 102
Stello, D., Chaplin, W. J., Bruntt, H., et al. 2009, ApJ, 700, 1589
Stello, D., Huber, D., Bedding, T. R., et al. 2013, ApJL, 765, L41
Stello, D., Saunders, N., Grunblatt, S., et al. 2022, MNRAS, 512, 1677
Stello, D., Zinn, J., Elsworth, Y., et al. 2017, ApJ, 835, 83
Taylor, M. B. 2005, ASPC, 347, 29
VanderPlas, J. T. 2018, ApJS, 236, 16
Viani, L. S., Basu, S., Chaplin, W. J., Davies, G. R., & Elsworth, Y. 2017, ApJ, 843, 11
Virtanen, P., Gommers, R., Oliphant, T. E., et al. 2020, NatMe, 17, 261
White, T. R., Bedding, T. R., Stello, D., et al. 2011, ApJ, 743, 161
Wu, T., Li, Y., & Hekker, S. 2014, ApJ, 781, 44
Yu, J., Huber, D., Bedding, T. R., et al. 2016, MNRAS, 463, 1297
Zhou, J., Bi, S., Yu, J., et al. 2024, ApJS, 271, 17